

## COMMUNICATION

[View Article Online](#)  
[View Journal](#) | [View Issue](#)Cite this: *Mater. Adv.*, 2021,  
2, 241Received 30th October 2020,  
Accepted 27th November 2020

DOI: 10.1039/d0ma00851f

[rsc.li/materials-advances](http://rsc.li/materials-advances)Gas-phase CO<sub>2</sub> electroreduction over  
Sn–Cu hollow fibers†Xiao Dong,<sup>a</sup> Guihua Li,<sup>a</sup> Wei Chen,<sup>a\*</sup> Chang Zhu,<sup>a</sup> Tong Li,<sup>a</sup>  
Yanfang Song,<sup>a</sup> Nannan Sun<sup>a</sup> and Wei Wei<sup>\*ab</sup>

CO<sub>2</sub> electroreduction to value-added chemicals by virtue of renewable electricity is significant for carbon emission abatement and renewable energy conversion/storage. Conventional CO<sub>2</sub> electroreduction occurring in aqueous solution or ionic liquid suffers from insufficient CO<sub>2</sub> solubility and a separation dilemma of the soluble products. In this work, we report that when using Sn–Cu hollow fiber electrodes, gas-phase CO<sub>2</sub> can be directly electroreduced into various multicarbon oxygenates. The faradaic efficiencies of acetaldehyde and acetone over a 0.3 wt% Sn–Cu hollow fiber electrode are 10 and 12% at the cell voltage of −1.4 V. The presence of an appropriate amount of SnO<sub>2</sub> nanoparticles decorated on a Cu hollow fiber surface not only facilitates the reaction kinetics with elevated current densities, but also improves the C–C coupling of intermediates, promoting the formation of multicarbon oxygenates.

The continuously elevating atmospheric CO<sub>2</sub> concentration which has arisen from tremendous fossil fuel consumption severely threatens the ecological environment.<sup>1,2</sup> Utilizing CO<sub>2</sub> as a safe, economic and sustainable C<sub>1</sub> resource via modern techniques to obtain value-added chemicals could contribute to carbon emission abatement, which is of great importance.<sup>3–6</sup> Comparing with the thermocatalytic conversion of CO<sub>2</sub>, which requires harsh conditions and a massive amount of energy, the CO<sub>2</sub> electroreduction conducted under mild conditions exhibits great application potentials.<sup>7,8</sup> Besides, the rapid-developing renewable electricity from wind and solar power would cause critical impacts on the transmission grid due to its randomness, intermittency and volatility, while CO<sub>2</sub> electroreduction could take in this low-grade renewable electricity in CO<sub>2</sub> conversion to obtain valuable chemicals.

Although CO<sub>2</sub> electrocatalysis has been widely studied for decades, the limited reaction kinetics constrained by the insufficient CO<sub>2</sub> solubility in liquid electrolyte (both aqueous solutions and ionic liquids),<sup>8–13</sup> and the separation dilemma of soluble products from liquid electrolyte (since the energy required to recover the products is higher than the energy stored in the produced molecules),<sup>7</sup> are still the two key issues. In spite of the many attempts of adopting gas-diffusion electrodes to alleviate the former issue by Sargent and other researchers, which could yield ethylene with a faradaic efficiency (FE) of 70%<sup>14</sup> and a 62% C<sub>2+</sub> product selectivity with a current density of 653 mA cm<sup>−2</sup>,<sup>15</sup> for example, the complicated fabrication procedures and multi-component configuration (active component|hydrophobic binder|conductive additions) of such gas-diffusion electrodes still hinder the industrial applications of CO<sub>2</sub> electrocatalysis.

In contrast, the gas-phase CO<sub>2</sub> electrocatalysis would allow easy product separation, and could get rid of the CO<sub>2</sub> solubility problems at the same time. Centi *et al.* first came up with the idea of gas-phase CO<sub>2</sub> electroreduction and the possibility to obtain long-chain hydrocarbon products with Pt/C catalysts and solid electrolyte Nafion<sup>®</sup>.<sup>16</sup> Kriescher *et al.* reported a Cu felt electrode with Fumapem membrane, obtaining mainly methane with FEs no more than 0.12%.<sup>17</sup> Recent studies from Gutiérrez-Guerra *et al.* used polybenzimidazoles (PBI) and Sterion<sup>®</sup> as the solid electrolyte for gas-phase CO<sub>2</sub> electroreduction at 90 °C, obtaining methanol and acetaldehyde with yields of 40 and 110 μmol g<sub>cat</sub><sup>−1</sup> h<sup>−1</sup> over Cu catalysts.<sup>18–20</sup> However, these studies are all based on conventional types of Cu-based electrodes, with unsatisfying overall efficiencies and insufficient value-added multicarbon products for the electroreduction of gas-phase CO<sub>2</sub>.

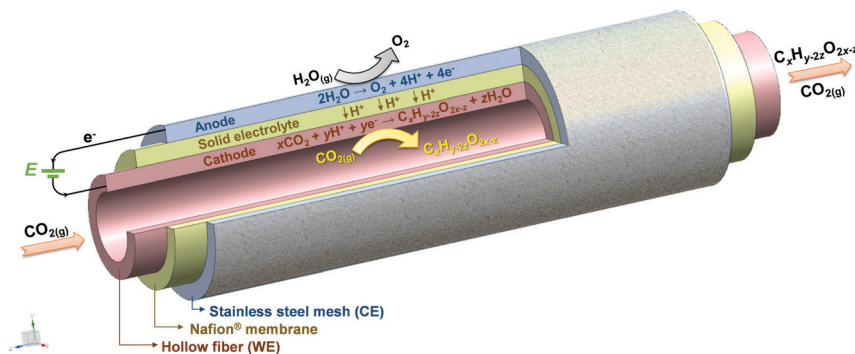
The porous hollow fiber (HF) electrode stands out as an alternative to the above-mentioned issues, which is fabricated via a combined phase-inversion and sintering process using commercial metal powder. This kind of self-supported gas-diffusion electrode can be adopted in electrochemical reaction systems without any binder. Its hierarchical pore

<sup>a</sup> CAS Key Laboratory of Low-Carbon Conversion Science and Engineering, Shanghai Advanced Research Institute, Chinese Academy of Sciences, Shanghai 201210,

P. R. China. E-mail: chenw@sari.ac.cn, weiwei@sari.ac.cn

<sup>b</sup> School of Physical Science and Technology, ShanghaiTech University, Shanghai 201210, P. R. China

† Electronic supplementary information (ESI) available. See DOI: 10.1039/d0ma00851f



**Scheme 1** Schematic diagrams of a gas-phase CO<sub>2</sub> electrochemical reaction system based on Sn-Cu hollow fibers as the working electrode.

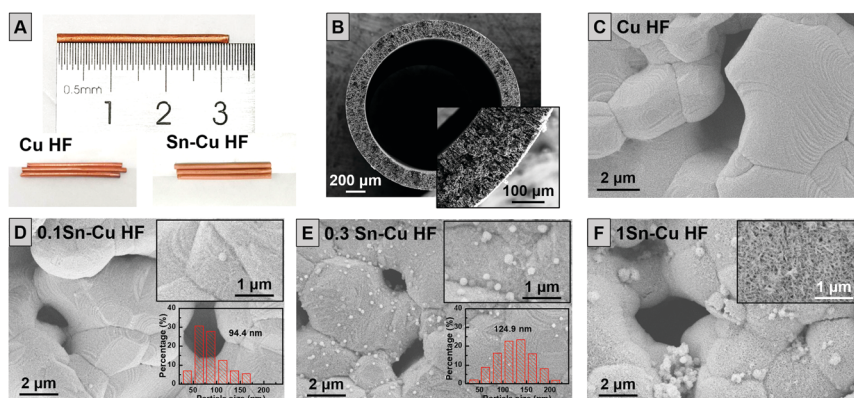


**Fig. 1** Morphology of hollow fiber electrodes. (A) Photographs of Cu HF and Sn-Cu HF electrodes, (B) cross-section SEM of Cu HF, and surface SEM of (C) Cu HF, (D) 0.1Sn-Cu HF, (E) 0.3Sn-Cu HF and (F) 1Sn-Cu HF electrodes. Insets show the partially enlarged SEM images of hollow fibers, as well as the nanoparticle size distributions on the sample surface.

structure, good stability and conductivity, have shown unique advantages in electrocatalysis applications,<sup>21–23</sup> and could be a suitable platform to study the gas-phase CO<sub>2</sub> electroreduction process.

On the other hand, Sn-based catalysts have been frequently used in CO<sub>2</sub> electroreduction due to its intrinsic high activity. Lei *et al.* reported confined Sn in graphene which exhibited high CO<sub>2</sub> electroreduction activities with 85% HCOOH FE at −0.48 V overpotential.<sup>24</sup> Bai *et al.* found that alloying Sn with Pd reached nearly 100% HCOOH FE *via* an optimal surface Pd-Sn-O configuration at the lowest overpotential of −0.26 V.<sup>25</sup> An *et al.* revealed that Sn<sup>2+</sup>/Sn<sup>4+</sup> species can reduce the overpotential and improve the HCOOH selectivity.<sup>26</sup> Liu *et al.* reported SnO<sub>2</sub> quantum wires with enhanced current density and improved HCOOH FE of over 80%.<sup>27</sup> Geng *et al.* found the Sn<sup>2+</sup> node in ZIF-8 can accelerate HCOOH formation with a FE of 74% and a total current density of 27 mA cm<sup>−2</sup>.<sup>28</sup> These findings indicate the great promotion of HCOOH formation by introducing Sn species in aqueous CO<sub>2</sub> electroreduction. However, during gas-phase CO<sub>2</sub> electroreduction, SnO<sub>2</sub> nanoparticles on the HF surface would play more important roles beyond facilitating the production of HCOOH species.

Here, a novel gas-phase CO<sub>2</sub> electrochemical reactor is developed based on Sn-Cu HF electrodes as illustrated in Scheme 1.

The porous Cu HF electrode is applied as a self-supported gas-diffusion electrode, while its surface is modified by Sn species *via* wet chemistry reduction with sodium citrate as the stabilizing agent and sodium borohydride (NaBH<sub>4</sub>) as the reductive agent (see the ESI† for details). The Sn-based catalysts always help the formation of formate,<sup>24–28</sup> while Cu-based catalysts are famous for the potential to promote C-C coupling and the formation of C<sub>2</sub> products such as ethylene and ethanol.<sup>8,29–31</sup> The loadings of Sn element in Sn-Cu HFs are controlled by varying the molar ratio between the SnCl<sub>2</sub> precursor and Cu HF. The obtained samples are denoted as xSn-Cu HFs, in which the *x* represents the loading of Sn element determined by ICP-OES (inductively coupled plasma-optical emission spectroscopy). Cu HF is also studied as the counterpart for comparison purposes.

As shown in Fig. 1A, the typical length of Cu HFs used in this work is about 3 cm with a color of light orange. The cross-section and surface scanning electron microscopy (SEM) images of Cu HF in Fig. 1B and C suggest the hollow structure of Cu HFs with an outer diameter of ~2 mm, as well as the porous fiber wall with a thickness of ~200 μm. The characteristic finger-like pores are dispersed in the fiber wall without any visible macrovoids, while abundant pores are formed with an average size of 2–5 μm on the smooth fiber surface. The porous



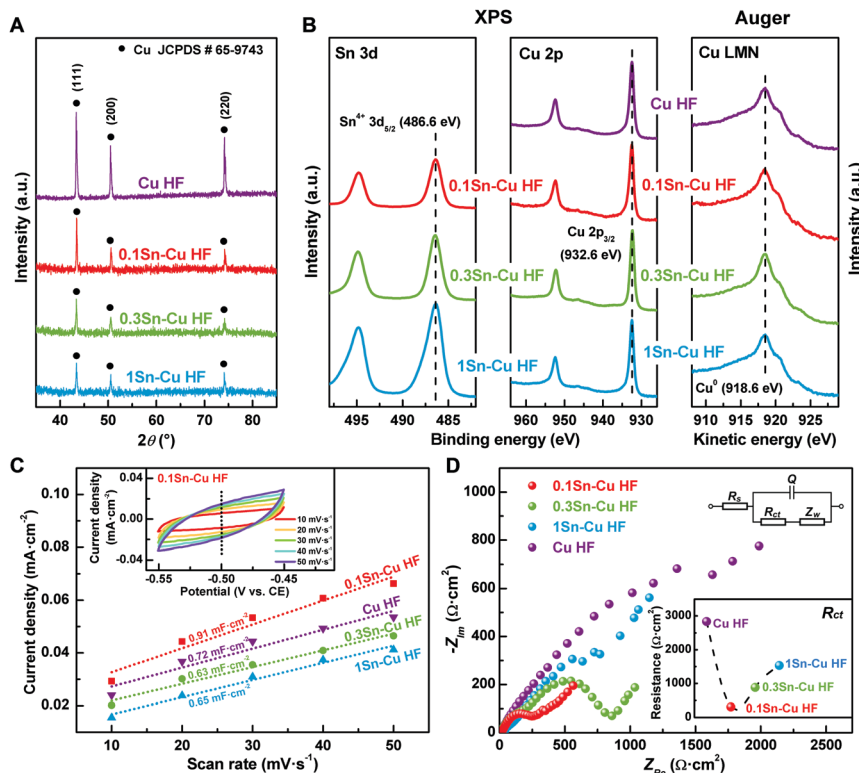


Fig. 2 Surface, bulk structure as well as electrochemical properties of hollow fiber electrodes. (A) XRD patterns, (B) Ag 3d, Cu 2p (XPS), Cu LMM (Auger) curves, (C) ECSA comparison, (D) EIS spectra and  $R_{ct}$  comparison of the as-prepared electrodes. Inset of (C) shows CV curves of 0.1Sn-Cu electrode in the range of  $-0.45$  to  $-0.55$  V vs. CE. Inset of (D) shows the equivalent circuit for EIS spectra fitting.

structure of Cu HF benefits the diffusion of gaseous reactants and products by providing plenty of pathways for mass transfer.<sup>21,22</sup> While the metallic nature of Cu HF guarantees sufficient electron conductivity, which would enlarge the three-phase boundary of reaction interfaces and facilitate the kinetics of  $\text{CO}_2$  electroreduction.<sup>21,22</sup> After the wet chemistry reduction preparation, no obvious appearance change could be observed for Sn-Cu HF in Fig. 1A. While the SEM images in Fig. 1D–F clearly indicate the formation of  $\text{SnO}_2$  nanoparticles or layer on the surface of Sn-Cu HF. With the elevated loading of Sn component, not only the amount of  $\text{SnO}_2$  nanoparticles increases, but also the average particle size enlarges from  $\sim 94$  nm for 0.1Sn-Cu HF (Fig. 1D) to  $\sim 125$  nm for 0.3Sn-Cu HF (Fig. 1E). For 1Sn-Cu HF, even a fabric-like  $\text{SnO}_2$  layer is formed, composed of dense  $\text{SnO}_2$  nanosheets vertically packed on the Cu HF surface (as shown in Fig. 1F).<sup>32</sup> While for all Sn-Cu HF samples, the abundant pore structure of Cu HF is still well-preserved, similar to other reported works.<sup>23</sup>

Fig. 2A shows the bulk structure of each HF sample characterized *via* X-ray diffraction (XRD) measurements. Peaks appearing at  $43.3$ ,  $50.4$  and  $74.1^\circ$  in all samples could be assigned to the characteristic peaks for (111), (200) and (220) planes of metallic Cu (JCPDS no. 65-9743), indicating that the main component of Cu HF and Sn-Cu HF is metallic Cu.<sup>33,34</sup> On the other hand, no diffraction peaks of all Sn-Cu electrodes corresponding to  $\text{SnO}_2$ ,  $\text{SnO}_x$  or other tin species<sup>23,25,26</sup> could

be observed, suggesting the nanoparticles are amorphous with insufficient loadings.<sup>35</sup>

In contrast to the bulk composition, the surface electronic states of catalysts can exert significant influence on the adsorption/desorption capacity as well as the catalytic performance. Fig. 2B shows the surface electronic states of Sn-Cu HF characterized *via* X-ray photoelectron spectroscopy (XPS). For Cu 2p spectra in the binding energy (BE) range of 925–965 eV, a Cu  $2p_{3/2}$  peak at 932.6 eV could be observed for each sample. Since the Cu  $2p_{3/2}$  peaks for both  $\text{Cu}^0$  and  $\text{Cu}^+$  would appear around this binding energy range (while the  $\text{Cu}^{2+}$   $2p_{3/2}$  peak locates at  $\sim 942$  eV), it is hard to distinguish the accurate electronic states of Cu with XPS results only.<sup>33,36</sup> Thus the Auger curves of Cu LMM in the kinetic energy (KE) range of 908–929 eV (*i.e.* 558–579 eV for BE) were collected. The Cu LMM peak of each sample appears at 918.6 eV, while that of  $\text{Cu}^+$  locates at 916.8 eV, suggesting that the  $\text{Cu}^0$  species exists on the surface of all HF samples.<sup>36</sup> For Sn 3d spectra in the BE range of 482–498 eV, Sn  $3d_{5/2}$  peaks at 486.6 eV could be observed for all Sn-Cu HF samples, which can be assigned to  $\text{Sn}^{4+}$  species rather than  $\text{Sn}^{2+}$  and  $\text{Sn}^0$  species with peaks at around 486.0 and 485.2 eV, respectively.<sup>23,25,26</sup> Due to the oxophilic intrinsic property of the tin element, the Sn component existed in the  $\text{SnO}_2$  state *via* the wet chemistry preparation route, as evidenced by the XPS results (Fig. 2B). This indicates the presence of  $\text{SnO}_2$  nanoparticles or layer on the Cu HF surface as observed in the SEM images. Tin oxide can be formed rapidly when metallic Sn is exposed to air

due to the oxophilicity of Sn,<sup>25</sup> while the relatively lower oxygen affinity of Cu would keep it from being oxidized.<sup>23</sup> Meanwhile, the intensity of Sn 3d<sub>5/2</sub> peaks increased with the elevated Sn component loading, indicating the growing amount of Sn<sup>4+</sup> species on the surface of Sn-Cu HF.

The enrichment of SnO<sub>2</sub> on the Sn-Cu HF surface could further be confirmed *via* the surface atomic ratio extracted from quantified XPS results, and the average atomic ratio in each Sn-Cu HF sample obtained from ICP analysis.<sup>35</sup> Table S1 (ESI†) presents the comparison between the surface atomic Sn/Cu ratio detected by XPS, (Sn/Cu)<sub>XPS</sub>, and the average atomic Sn/Cu ratio from ICP analysis, (Sn/Cu)<sub>ICP</sub>, for Sn-Cu HF samples. It is clear that the (Sn/Cu)<sub>XPS</sub> numbers are a hundred times that of (Sn/Cu)<sub>ICP</sub>, demonstrating that the SnO<sub>2</sub> deposited *via* wet chemistry reduction preparation is enriched at the surface of Sn-Cu HF. It is also reported that SnO<sub>x</sub> with a valence of +4 can play an essential role in the CO<sub>2</sub> electroreduction process.<sup>37</sup> This abundance of oxide species existing on the Cu electrode surface would affect the CO<sub>2</sub> electroreduction significantly.

The gas-phase CO<sub>2</sub> electrochemical reaction system based on a hollow fiber electrode is shown in Scheme 1 (see the ESI† for details). A single hollow fiber is used as the working electrode (WE) and support. A Nafion<sup>®</sup> membrane is covered on the surface of the hollow fiber as the solid electrolyte and diaphragm between the anode and cathode. Stainless steel mesh (SSM) is then deployed on the surface of Nafion<sup>®</sup>, functioning as the counter electrode (CE). Both electrochemical characterization and reaction performance tests were conducted on this reaction system.

The electrochemical active surface areas (ECSAs) of Sn-Cu HF electrodes are determined based on their double-layer capacitances *via* a cyclic voltammetry (CV) method. All CV profiles (Fig. S2, ESI† and the inset in Fig. 2C) exhibit nearly symmetrical shapes in the range of −0.45 to −0.55 V vs. CE,

indicating the capacitive behaviors of double-layer capacitance for Sn-Cu HF electrodes. The cathodic and anodic current densities are obtained from the double layer charge/discharge CV curves at −0.5 V vs. CE. The double layer capacitance (*C*<sub>dl</sub>), which is directly proportional to the ECSA, is then calculated by averaging the absolute values of cathodic and anodic current density slopes *via* linear fits.<sup>22</sup> The obtained *C*<sub>dl</sub> values are 0.72, 0.91, 0.63 and 0.65 mF cm<sup>−2</sup> for Cu HF, 0.1Sn-Cu HF, 0.3Sn-Cu HF and 1Sn-Cu HF, respectively (as shown in Fig. 2C). This implies that the ECSA of 0.1Sn-Cu HF is the largest, while the ECSAs of 0.3Sn-Cu HF and 1Sn-Cu HF are quite similar to each other.

The electrochemical impedance spectra (EIS) of Sn-Cu HF electrodes at −1.4 V vs. CE, as well as the corresponding charge transfer resistances (*R*<sub>ct</sub>) are shown in Fig. 2D, which are obtained *via* the equivalent circuit shown in the inset. The *R*<sub>ct</sub> of Cu HF is 2.8 kΩ cm<sup>2</sup>, which is much larger than those of Sn-Cu HF. The *R*<sub>ct</sub> increases monotonically from 0.3 kΩ cm<sup>2</sup> for 0.1Sn-Cu HF, to 0.9 kΩ cm<sup>2</sup> for 0.3Sn-Cu HF and 1.5 kΩ cm<sup>2</sup> for 1Sn-Cu HF with the increase of SnO<sub>2</sub> content. This phenomenon indicates that the presence of few SnO<sub>2</sub> nanoparticles significantly promotes the reaction kinetics for their high activities, leading to smaller *R*<sub>ct</sub> corresponding to electrochemical reaction resistance. SnO<sub>2</sub> has been reported for its efficient, selective, and durable performance for CO<sub>2</sub> electroreduction.<sup>24–28</sup> On the other hand, although SnO<sub>2</sub> is known as a p-type semiconductor with relatively fast electron transportation, the electronic conductivity of SnO<sub>2</sub> is still far below that of the metallic conductor. Therefore, the higher amount of SnO<sub>2</sub> nanoparticles and even SnO<sub>2</sub> layer on the Cu HF surface would hamper the charge transfer steps of electrochemical reaction due to the semiconductive nature of SnO<sub>2</sub>, leading to increased *R*<sub>ct</sub>.<sup>25</sup>

Fig. 3 shows the gas-phase CO<sub>2</sub> electroreduction performance of hollow fiber electrodes at different potentials. No

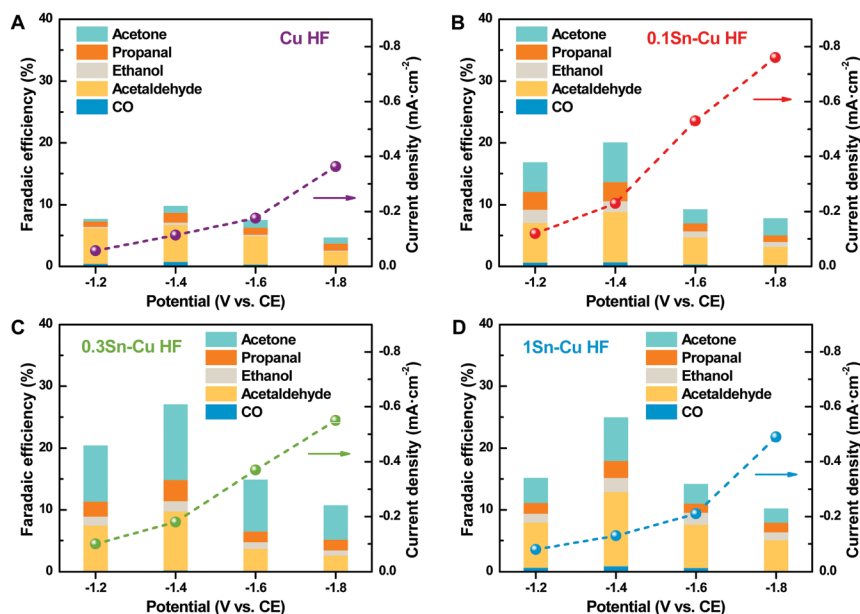


Fig. 3 Electrochemical reaction performance of hollow fiber electrodes. Faradaic efficiencies and current densities of (A) Cu HF, (B) 0.1Sn-Cu HF, (C) 0.3Sn-Cu HF and (D) 1Sn-Cu HF electrodes for gas-phase CO<sub>2</sub> electroreduction at different potentials.





reduction products are observed under open circuit voltage (OCV), *i.e.*, with no current applied, while a large variety of products is obtained under polarization conditions. Acetaldehyde could be observed as one of the main products for all electrodes with several other C<sub>1</sub>–C<sub>3</sub> products, while no H<sub>2</sub> from the competitive H<sub>2</sub> evolution reaction could be detected in the examined conditions, which is consistent with the results of former gas-phase CO<sub>2</sub> electroreduction studies.<sup>16–20</sup> The gas-phase electrocatalytic reduction of CO<sub>2</sub> is a complex multistep reaction involving shared intermediates and multiple reaction pathways.<sup>19,20</sup> The formation of the different products can be described by a general reaction as shown in Scheme 1 for the cathodic reaction of CO<sub>2</sub> and H<sup>+</sup> with e<sup>−</sup>.

For the Cu HF electrode, the current densities are −0.06, −0.11, −0.18 and −0.36 mA cm<sup>−2</sup> respectively, at working potentials of −1.2, −1.4, −1.6 and −1.8 V *vs.* CE. Acetaldehyde is the main reduction product at all conditions, which is in agreement with previous studies of gas-phase CO<sub>2</sub> electroreduction.<sup>18–20</sup> At the potential of −1.4 V *vs.* CE, the total FE for all products is about 10%, while ~25 nmol cm<sup>−2</sup> h<sup>−1</sup> acetaldehyde is formed with a FE of around 6%. Table S2 (ESI<sup>†</sup>) summarizes the gas-phase CO<sub>2</sub> electroreduction performances on Cu-based catalysts reported in the literature. Although Gutiérrez-Guerra *et al.* obtained 55 nmol cm<sup>−2</sup> h<sup>−1</sup> acetaldehyde production (110 μmol g<sub>cat</sub><sup>−1</sup> h<sup>−1</sup> with a catalyst loading of 0.5 mg cm<sup>−2</sup>) at a higher temperature and potential (90 °C, −2.75 V, −1.6 mA cm<sup>−2</sup>), the FE of acetaldehyde is only 1%.<sup>18</sup> This phenomenon indicates that the gas-phase CO<sub>2</sub> electroreduction system based on HF electrodes could be more efficient, and would be a better platform for developing novel electrocatalysts.

For Sn–Cu HF electrodes, a greater amount of C<sub>3</sub> products such as propanal and acetone could be observed. The current densities for 0.1Sn–Cu HF are greatly improved to −0.12, −0.23, −0.53 and −0.76 mA cm<sup>−2</sup>, respectively, at each working potential. The small amount of SnO<sub>2</sub> nanoparticles deposited on the Cu HF surface facilitates the kinetics of gas-phase CO<sub>2</sub> electroreduction, leading to the elevated current densities and the reduced reaction resistance (Fig. 2D). Besides, the total FE for all reduction products is about 20%, among which 34 nmol cm<sup>−2</sup> h<sup>−1</sup> acetone is formed with a FE of around 6% at −1.4 V *vs.* CE. Although the proportion of acetone in all products has been increased, acetaldehyde is still the main product with a FE of ~8%. The yield of acetaldehyde leaps to 70 nmol cm<sup>−2</sup> h<sup>−1</sup>, which is higher than those reported in the literature as shown in Table S2 (ESI<sup>†</sup>),<sup>18–20</sup> indicating the promoted activities for both C<sub>2</sub> and C<sub>3</sub> products with few deposited SnO<sub>2</sub> nanoparticles on the Cu HF electrode surface (0.1 wt%).

The current densities for 0.3Sn–Cu HF and 1Sn–Cu HF are not further increased. At a working potential of −1.2, −1.4, −1.6 and −1.8 V *vs.* CE, the current densities for 0.3Sn–Cu HF drop to −0.10, −0.18, −0.37 and −0.55 mA cm<sup>−2</sup> respectively, while those for 1Sn–Cu HF keep decreasing to −0.08, −0.13, −0.21 and −0.49 mA cm<sup>−2</sup>, but are still higher than those of Cu HF. The current density changes are consistent with the trend of *R*<sub>ct</sub> in Fig. 2D. The larger amount of SnO<sub>2</sub> nanoparticles and

even SnO<sub>2</sub> layer on the Cu HF surface with its semiconductive property hinders the charge transfer steps. However, the total FEs for all products on both electrodes are elevated to about 27% and 24%. The increased SnO<sub>2</sub> nanoparticle deposition (0.3 wt%) further promotes the production of acetone and restrains the formation of acetaldehyde. For 0.3Sn–Cu HF, the production of acetaldehyde reduces to 64 nmol cm<sup>−2</sup> h<sup>−1</sup> with a FE of 10% at −1.4 V *vs.* CE, while in contrast that of acetone rises to 51 nmol cm<sup>−2</sup> h<sup>−1</sup> with a FE of 12%, indicating that the highly dispersed SnO<sub>2</sub> nanoparticles would facilitate further C–C coupling of C<sub>2</sub> intermediates on the Cu surface. While for 1Sn–Cu HF the acetaldehyde production rate keeps reducing to 58 nmol cm<sup>−2</sup> h<sup>−1</sup> with a FE of 12%, and that of acetone also drops back to 18 nmol cm<sup>−2</sup> h<sup>−1</sup> with a FE of 6%. The excessive SnO<sub>2</sub> loading (1 wt%) leads to the formation of a poorly conductive SnO<sub>2</sub> layer on the Cu HF surface, hindering the charge transfer procedures, resulting in the downward yields for both acetaldehyde and acetone.

It is believed that the sites with SnO<sub>2</sub> particles located on the Cu HF surface are the active centers. As illustrated in Fig. 3, although the Cu HF electrode itself shows some electrochemical activity for gas-phase CO<sub>2</sub> reduction to multicarbon products, the current density and their faradaic efficiencies are much lower compared to the Sn-modified electrodes. Introducing Sn species into aqueous CO<sub>2</sub> electroreduction usually promotes the formation of HCOOH,<sup>24–28</sup> while during gas-phase CO<sub>2</sub> electroreduction, SnO<sub>2</sub> nanoparticles on the Cu surface play more important roles. The HCOOH species facilitated by virtue of SnO<sub>2</sub> are further converted into \*CHO intermediates at the SnO<sub>2</sub>/Cu interface, which subsequently dimerize into C<sub>2</sub> intermediate glyoxal (CHO)<sub>2</sub>.<sup>38,39</sup> The next steps include the formation of \*COCHO and \*CHCOH to obtain acetaldehyde and ethanol,<sup>38,39</sup> while the adsorbed \*CHCOH could further undergo intermolecular C–C coupling with an adjacent \*CHO to form propanal and acetone.<sup>39,40</sup> Thus, the CO<sub>2</sub> activation and subsequent coupling of the intermediates are enhanced by virtue of the decoration of SnO<sub>2</sub> on Cu surfaces, resulting in the improvement of the multicarbon product faradaic efficiencies. However, excess amount of SnO<sub>2</sub> hinders the performance greatly on the 1Sn–Cu HF electrode, implying a slowing of charge transfer due to the dielectric property of the SnO<sub>2</sub> layer. Therefore, the formation of multicarbon products with relatively high efficiency on the appropriate 0.3Sn–Cu HF electrode can be attributed to the synergistic effect between SnO<sub>2</sub> particles and Cu surface, which favour the HCOOH intermediate formation and the subsequent coupling of the key intermediate \*CHO.

## Conclusions

In summary, a novel gas-phase CO<sub>2</sub> electroreduction system is developed based on the Sn–Cu HF electrode in this work, taking the unique advantages of HFs such as large surface area, adjustable pore structure, good chemical stability and conductivity. The presence of an appropriate amount of SnO<sub>2</sub> nanoparticles



decorated on the Cu HF surface *via* NaBH<sub>4</sub> reduction preparation could optimize the surface active structure for the gas-phase CO<sub>2</sub> electroreduction, which not only facilitates the reaction kinetics to increase the current densities of CO<sub>2</sub> electroreduction, but also improves the C–C coupling of intermediates on the Cu HF surface, promoting the formation of multicarbon oxygenates, especially acetaldehyde and acetone. At a cell voltage of  $-1.4$  V, the yields of acetaldehyde and acetone over the 0.3Sn–Cu HF electrode are 64 and 51 nmol cm<sup>-2</sup> h<sup>-1</sup> with FEs of 10 and 12%, respectively. These results highlight the advantages of Sn–Cu HF electrodes in efficient gas-phase CO<sub>2</sub> electroreduction to obtain multicarbon oxygenate products, and inspire the design and development of novel electrocatalytic systems.

## Conflicts of interest

There are no conflicts to declare.

## Acknowledgements

This work was financially supported by the National Natural Science Foundation of China (no. 91745114 and 21802160), the Ministry of Science and Technology of China (no. 2016YFA0202800 and 2018YFB0604700), the Shanghai Sailing Program (no. 18YF1425700), the Hundred Talents Program of Chinese Academy of Sciences and the Shanghai Functional Platform for Innovation Low Carbon Technology.

## References

- 1 M. Christophe and E. Paul, *Nature*, 2015, **517**, 187–190.
- 2 J. Tollefson, *Nature*, 2015, **520**, 14–15.
- 3 G. A. Olah, G. K. S. Prakash and G. Alain, *J. Am. Chem. Soc.*, 2011, **133**, 12881–12898.
- 4 W. I. A. Sadat and L. A. Archer, *Sci. Adv.*, 2016, **2**, e1600968.
- 5 Z. Huang, J. G. Uranga, S. Zhou, H. Jia, Z. Fei, Y. Wang, F. D. Bobbink, Q. Lu and P. J. Dyson, *J. Mater. Chem. A*, 2018, **6**, 20916–20925.
- 6 G. Xu, H. Zhang, J. Wei, H. X. Zhang, X. Wu, Y. Li, C. Li, J. Zhang and J. Ye, *ACS Nano*, 2018, **12**, 5333–5340.
- 7 E. V. Kondratenko, G. Mul, J. Baltrusaitis, G. O. Larrazabal and J. Perez-Ramirez, *Energy Environ. Sci.*, 2013, **6**, 3112–3135.
- 8 D. D. Zhu, J. L. Liu and S. Z. Qiao, *Adv. Mater.*, 2016, **28**, 3423–3452.
- 9 Z. Sun, T. Ma, H. Tao, Q. Fan and B. Han, *Chemistry*, 2017, **3**, 560–587.
- 10 S. Nitopi, E. Bertheussen, S. B. Scott, X. Liu, A. K. Engstfeld, S. Horch, B. Seger, I. E. L. Stephens, K. Chan, C. Hahn, J. K. Nørskov, T. F. Jaramillo and I. Chorkendorff, *Chem. Rev.*, 2019, **119**, 7610–7672.
- 11 M. B. Ross, P. De Luna, Y. Li, C.-T. Dinh, D. Kim, P. Yang and E. H. Sargent, *Nat. Catal.*, 2019, **2**, 648–658.
- 12 N. Hollingsworth, S. F. R. Taylor, M. T. Galante, J. Jacquemin, C. Longo, K. B. Holt, N. H. D. Leeuw and C. Hardacre, *Angew. Chem., Int. Ed.*, 2015, **54**, 14164–14168.
- 13 M. Alvarez-Guerra, J. Albo, E. Alvarez-Guerra and Á. Irabien, *Energy Environ. Sci.*, 2015, **8**, 2574–2599.
- 14 C.-T. Dinh, T. Burdyny, M. G. Kibria, A. Seifitokaldani, C. M. Gabardo, F. P. García de Arquer, A. Kiani, J. P. Edwards, P. De Luna, O. S. Bushuyev, C. Zou, R. Quintero-Bermudez, Y. Pang, D. Sinton and E. H. Sargent, *Science*, 2018, **360**, 783–787.
- 15 J.-J. Lv, M. Jouny, W. Luc, W. Zhu, J.-J. Zhu and F. Jiao, *Adv. Mater.*, 2018, **30**, 1803111.
- 16 G. Centi, S. Perathoner, G. Win and M. Gangeri, *Green Chem.*, 2007, **9**, 671–678.
- 17 S. M. A. Kriescher, K. Kugler, S. S. Hosseiny, Y. Gendel and M. Wessling, *Electrochem. Commun.*, 2015, **50**, 64–68.
- 18 N. Gutiérrez-Guerra, L. Moreno-López, J. C. Serrano-Ruiz, J. L. Valverde and A. de Lucas-Consuegra, *Appl. Catal., B*, 2016, **188**, 272–282.
- 19 N. Gutiérrez-Guerra, J. L. Valverde, A. Romero, J. C. Serrano-Ruiz and A. de Lucas-Consuegra, *Electrochem. Commun.*, 2017, **81**, 128–131.
- 20 N. Gutiérrez-Guerra, J. A. González, J. C. Serrano-Ruiz, E. López-Fernández, J. L. Valverde and A. de Lucas-Consuegra, *J. Energy Chem.*, 2019, **31**, 46–53.
- 21 R. Kas, K. K. Hummadi, R. Kortlever, P. de Wit, A. Milbrat, M. W. J. Luiten-Olieman, N. E. Benes, M. T. M. Koper and G. Mul, *Nat. Commun.*, 2016, **7**, 10748–10754.
- 22 Z. Guo, W. Chen, Y. Song, X. Dong, G. Li, W. Wei and Y. Sun, *Chin. J. Catal.*, 2020, **41**, 1067–1072.
- 23 H. Rabiee, X. Zhang, L. Ge, S. Hu, M. Li, S. Smart, Z. Zhu and Z. Yuan, *ACS Appl. Mater. Interfaces*, 2020, **12**, 21670–21681.
- 24 F. Lei, W. Liu, Y. Sun, J. Xu, K. Liu, L. Liang, T. Yao, B. Pan, S. Wei and Y. Xie, *Nat. Commun.*, 2016, **7**, 12697–12705.
- 25 X. Bai, W. Chen, C. Zhao, S. Li, Y. Song, R. Ge, W. Wei and Y. Sun, *Angew. Chem., Int. Ed.*, 2017, **56**, 12219–12223.
- 26 X. An, S. Li, A. Yoshida, Z. Wang, X. Hao, A. Abudula and G. Guan, *ACS Sustainable Chem. Eng.*, 2019, **7**, 9360–9368.
- 27 S. Liu, J. Xiao, X. F. Lu, J. Wang, X. Wang and X. W. Lou, *Angew. Chem., Int. Ed.*, 2019, **58**, 8499–8503.
- 28 W. Geng, W. Chen, G. Li, X. Dong, Y. Song, W. Wei and Y. Sun, *ChemSusChem*, 2020, **13**, 4035–4040.
- 29 D. Ren, Y. Deng, A. D. Handoko, C. S. Chen, S. Malkhandi and B. S. Yeo, *ACS Catal.*, 2015, **5**, 2814–2821.
- 30 Q. Li, W. Zhu, J. Fu, H. Zhang, G. Wu and S. Sun, *Nano Energy*, 2016, **24**, 1–9.
- 31 Y. Song, R. Peng, D. K. Hensley, P. V. Bonnesen, L. Liang, Z. Wu, H. M. Meyer, M. Chi, C. Ma, B. G. Sumpter and A. J. Rondinone, *ChemistrySelect*, 2016, **1**, 6055–6061.
- 32 F. Li, L. Chen, G. P. Knowles, D. R. MacFarlane and J. Zhang, *Angew. Chem., Int. Ed.*, 2017, **56**, 505–509.
- 33 S. Rasul, D. H. Anjum, A. Jedidi, Y. Minenkov, L. Cavallo and K. Takanabe, *Angew. Chem., Int. Ed.*, 2015, **127**, 2174–2178.
- 34 M. Wu, C. Zhu, K. Wang, G. Li, X. Dong, Y. Song, J. Xue, W. Chen, W. Wei and Y. Sun, *ACS Appl. Mater. Interfaces*, 2020, **12**, 11562–11569.
- 35 X. Dong, P. Zheng, A. G. Zheng, H. F. Li, G. F. Xia, M. F. Li, R. Y. Zheng and B. Q. Xu, *Catal. Today*, 2018, **316**, 162–170.
- 36 T. Yano, M. Ebizuka, S. Shibata and M. Yamane, *J. Electron Spectrosc. Relat. Phenom.*, 2003, **131–132**, 133–144.



- 37 Y. Li, J. Qiao, X. Zhang, T. Lei, A. Girma, Y. Liu and J. Zhang, *ChemElectroChem*, 2016, **3**, 1618–1628.
- 38 A. J. Garza, A. T. Bell and M. Head-Gordon, *ACS Catal.*, 2018, **8**, 1490–1499.
- 39 L. Wang, W. Chen, D. Zhang, Y. Du, R. Amal, S. Qiao, J. Wu and Z. Yin, *Chem. Soc. Rev.*, 2019, **48**, 5310–5349.
- 40 S. Munir, A. R. Varzeghani and S. Kaya, *Sustainable Energy Fuels*, 2018, **2**, 2532–2541.

